

# Arterial input function calculation in dynamic contrast-enhanced MRI: an in vivo validation study using co-registered contrast-enhanced ultrasound imaging

Hatef Mehrabian · Chaitanya Chandrana · Ian Pang ·  
Rajiv Chopra · Anne L. Martel

Received: 17 October 2011 / Revised: 7 January 2012 / Accepted: 26 January 2012  
© European Society of Radiology 2012

## Abstract

**Objectives** Developing a method of separating intravascular contrast agent concentration to measure the arterial input function (AIF) in dynamic contrast-enhanced magnetic resonance imaging (DCE-MRI) of tumours, and validating its performance in phantom and in vivo experiments.

**Methods** A tissue-mimicking phantom was constructed to model leaky tumour vasculature and DCE-MR images of this phantom were acquired. An in vivo study was performed using tumour-bearing rabbits. Co-registered DCE-MRI and contrast-enhanced ultrasound (CEUS) images were acquired. An independent component analysis (ICA)-based method was developed to separate the intravascular component from DCE-MRI. Results were validated by comparing the time-intensity curves with the actual phantom and in vivo curves.

**Results** Phantom study: the AIF extracted using ICA correlated well with the true intravascular curve. In vivo study: the AIFs extracted from DCE-MRI using ICA were very close to the true AIF. Intravascular component images were very similar to the CEUS images. The contrast onset times and initial wash-in slope of the ICA-derived AIF showed good agreement with the CEUS curves.

**Conclusion** ICA has the potential to separate the intravascular component from DCE-MRI. This could eliminate the requirement for contrast medium uptake measurements in a

major artery and potentially result in more accurate pharmacokinetic parameters.

## Key Points

- Tumour response to therapy can be inferred from pharmacokinetic parameters.
- Arterial input function (AIF) is required for pharmacokinetic modelling of tumours.
- Independent component analysis has the potential to measure AIF inside the tumour.
- AIF measurement is validated using contrast enhanced ultrasound and phantoms.

**Keywords** Pharmacokinetics · Independent component analysis (ICA) · Arterial input function (AIF) · Dynamic contrast-enhanced MRI (DCE-MRI) · Contrast-enhanced ultrasound (CEUS)

## Introduction

Advances in our understanding of cancer biology have resulted in the development of novel therapeutics with the capability to target diseases based on molecular characteristics. Given the specificity and cost of these approaches, proper selection of patients who would benefit from these treatments is essential. In addition, the ability to determine the response of a tumour to treatment early in the course of therapy is essential, in order to adjust the course of treatment [1, 2]. Currently, imaging measurements of tumour size and evaluation of serum markers are the two main approaches used clinically to assess therapeutic response. With respect to serum marker monitoring, only a small number of tumours produce specific markers at sufficient level to be used for monitoring. Consequently, the response evaluation criterion in solid tumours (RECIST) has become the standard approach

---

The preliminary results of this study were presented in the IEEE International Symposium on Biomedical Imaging (ISBI): From Nano to Macro, Chicago, Illinois, USA, March 30–April 2, 2011.

---

H. Mehrabian (✉) · C. Chandrana · I. Pang · R. Chopra ·  
A. L. Martel  
Department of Medical Biophysics,  
Sunnybrook Research Institute, University of Toronto,  
2075 Bayview Avenue,  
Toronto, ON M4N 3M5, Canada  
e-mail: hatef.mehrabian@sri.utoronto.ca

to evaluate tumour response. Despite its broad adoption, this criterion is not always correct and has some limitations, as some molecular targeted agents may result in improved clinical response while making no significant change in tumour size [3]. Thus, there has been significant interest in functional and molecular imaging techniques such as positron emission tomography with  $^{18}\text{F}$ -fluorodeoxyglucose (FDG-PET) [4] and magnetic resonance imaging (MRI: non-contrast,  $T_1/T_2$ -weighted, diffusion-weighted, perfusion-weighted and dynamic contrast-enhanced) [5, 6].

A conventional dynamic contrast-enhanced (DCE)-MRI study which involves intravenous administration of a low molecular weight contrast agent, followed by repeated imaging of the tissue for at least 3 min [2] to track its passage through tumour vasculature into the extravascular extracellular space (EES), provides information about blood volume and tumour microvascular permeability. Vascular properties of tumour tissue can be quantified by assessing the kinetics of the contrast agent [7, 8]. Pharmacokinetic (PK) modelling can be used to provide quantitative information such as the volume transfer rate ( $k^{\text{trans}}$ ) and extravascular extracellular volume fraction ( $v_e$ ); these model parameters provide information about perfusion and permeability of tumour vasculature [5] and have been found to be related to prognostic factors [9]. As tissue vasculature can be assessed by DCE-MRI, its role in assessing anti-angiogenic and anti-vascular therapies is increasing [10–12].

The accumulation and wash-out of contrast agent in the EES of the tumour media is described by a PK model [7]. Several models have been introduced for PK analysis such as the Tofts model and extended Tofts model that assume the contrast agent is instantaneously distributed and is well mixed in each compartment [13] and the AATH model that assumes the contrast concentration in the EES space is defined as a function of transit time and the distance along the capillary [14]. A fundamental step in PK modelling that is common amongst all parametric models is determining the contrast agent concentration in the intravascular space (tumour arterial input function) [15]. This signal is usually inseparable from the extravascular contrast concentration due to the partial volume effect, the heterogeneous structure of tumour vasculature and low resolution of images that makes finding purely intravascular areas inside the tumour extremely difficult [16]. Thus, there is no method to directly measure the actual arterial input function (AIF) inside the tumour in these studies.

In order to estimate the arterial input function (AIF), it is common to use the contrast agent concentration in an artery that is anatomically adjacent to the tumour [17], a standard AIF which usually takes the form of a bi-exponential curve [8] and its parameters are measured experimentally [18], a population-averaged AIF [19] or a reference-tissue-based AIF which tries to estimate AIF from the concentration of contrast agent in a normal tissue with known physiological properties [20]. The concentration in the whole tumour region is considered as

either extravascular (Tofts model) or a parameter is introduced (extended Tofts model) to account for the fraction that is intravascular (blood plasma volume per unit volume of tissue,  $v_p$ ). Some assumptions in the choice of these AIFs are: (1) the chosen AIF is the feeding vessel to the tumour, (2) no other artery is supplying blood and consequently contrast agent to the tumour and (3) there is no delay, i.e. contrast agent arrives in the artery and the tumour at the same time or an unknown ( $\omega$ ) is added to the system to account for the delay. These unknown parameters make solving the system complex and sensitive to noise, such that although introducing extra parameters make the model more accurate, due to increased complexity and instability of the system of equations that has to be solved, the performances of different models are similar and there is no optimal number of model parameters [7].

An independent component analysis (ICA)-based method is proposed to measure the AIF in the tumour and separate it from the extravascular signal. Such a separation does not require an artery, accounts for variability between subjects and simplifies the PK modelling since some of the unknown parameters are eliminated.

The objectives of this study were: (1) to optimise the ICA algorithm for use with DCE-MRI data and to develop a method of calculating the AIF by the appropriate combination of ICA components, and (2) to evaluate the ability of the resulting method to separate AIF in tumour tissue from signal enhancement resulting from diffusion of contrast agent into the extravascular space. The performance of the method was evaluated in both tissue-mimicking phantoms using the out-flow signal as a reference and in vivo implanted tumours in a rabbit model using co-registered contrast-enhanced ultrasound (CEUS) imaging as an intravascular reference signal.

## Materials and methods

The MRI signal recorded in each voxel during passage of a contrast agent is a superposition of the signal generated in the intravascular and extravascular spaces in that voxel. These spaces are spatially independent, i.e. they have no overlap anatomically, and their contrast uptake and, accordingly, their signal intensity changes are different (note that these signals are not temporally independent, as their contrast agent concentration curves are correlated). The signal in each voxel, and consequently each frame, can be treated as a linear composition of the signal in the two spaces [21, 22]. These characteristics satisfy the assumptions for independent component analysis and, thus, ICA can potentially be used to separate them [23].

### Separation using independent component analysis

Independent component analysis (ICA) is a statistical signal processing approach that can separate different structures of

a dynamic image dataset from the raw image dataset that is a mixture of these structures. The separation is performed assuming these structures are mutually independent in spatial domain, without assuming any knowledge of the mixing coefficients [24]. The core idea of ICA is motivated from blind source separation problem for data model of the form

$$X = AS \tag{1}$$

where  $X=[x_1, x_2, \dots, x_N]^T$  is a matrix of the  $N$  frames of the dynamic dataset and  $S=[s_1, s_2, \dots, s_M]^T$  is a matrix containing the  $M$  structures that are known as independent components or ICs (usually  $M \leq N$ ). In the current study,  $X$  represents the DCE-MRI time series of images and  $S$  represents the intravascular, extravascular, and any other contributions to the acquired images, e.g. noise.  $A \in \mathbb{R}^{N \times M}$  is the weighting matrix whose columns are the time-intensity curves of each component (e.g. intravascular and extravascular). The aim of ICA is to estimate the independent components  $S$  and the weighting matrix  $A$  having the observed mixture signals  $X$ .

The independent components in ICA can only be estimated up to a scaling and the order in which they are extracted can change. ICA algorithms try to find a separating matrix  $W \in \mathbb{R}^{M \times N}$  and estimate the IC matrix  $Y=[y_1, y_2, \dots, y_M]^T$  such that:

$$Y = WX \tag{2}$$

where rows of  $Y$  are statistically independent. The matrix  $Y$  is only different from matrix  $S$  in the order of its rows (the ICs) and their scaling. The scaling problem is addressed in the next section and the order of ICs does not affect our analysis as all ICs are extracted in our method and the intravascular components are identified based on their time-intensity curves.

Dimensionality reduction was performed as a pre-processing step in order to reduce noise. Principal component analysis (PCA) was performed on the dataset and the significant eigenvalues (the eigenvalues that were bigger than 0.1% of the largest eigenvalue) that accounted for 99.9% of the information in the dataset were kept.

Based on the central limit theorem, the distribution of a sum of independent random variables tends towards a Gaussian distribution [25]. Thus, to find the independent components of an observed dataset, one has to maximise the non-Gaussianity of the extracted components. The ICA problem is formulated as:

$$J(y) = \max \left[ \rho(E\{G(y)\} - E\{G(y_{Gauss})\})^2 \right] \tag{3}$$

Where  $\rho$  is a positive constant,  $G(\cdot)$  is a non-quadratic function and  $E\{\cdot\}$  is the expectation operator [26, 27]. We used the skewness function for  $G(\cdot)$  in our algorithm:

$$G(y) = y^3 \tag{4}$$

The Newton method was used in our ICA algorithm to maximise Eq. 3 [28, 29]; the ICs were estimated one at a time and each IC was orthogonalised to the previously estimated one to avoid overlap between them [26].

ICA was applied to the dataset after dimensionality reduction and the number of extracted independent components (IC) was equal to the number of significant eigenvalues. The intravascular components were selected heuristically such that the curves that had a uniform pre-contrast uptake phase, an uptake phase in which the intensity increased rapidly and a wash-out phase in which the intensity dropped to less than 60% of the peak value after the peaks were selected as the intravascular components. This heuristic criterion was selected, as we observed throughout our study that the time-intensity curves of the components that behaved like an intravascular signal dropped to less than 60% of their peak value after 4.5 min.

### AIF calculation

As ICA is a data-driven algorithm that makes no assumptions about the physiology, some physiological structures might be split into a number of ICs. These ICs are combined to generate the spatial and temporal signals. Assuming  $k$  ICs are identified to be intravascular, the intravascular time-intensity curve was calculated using Eq. 5:

$$c_{intravascular} = \frac{C_{1\_ICA} \times \text{sum}(im_{1\_ICA}) + \dots + C_{k\_ICA} \times \text{sum}(im_{k\_ICA})}{\text{number of voxels}_1 + \dots + \text{number of voxels}_k} \tag{5}$$

where,  $\text{number of voxels}_1 = \text{number of voxels where } \{im_{i\_ICA} \geq 0.5 \max(im_{i\_ICA})\}$ , and  $C_{i\_ICA}$  is the time-intensity curve corresponding to the  $i$ th intravascular component and  $im_{i\_ICA}$  is its corresponding image.

### Ultrasound imaging

Contrast enhanced ultrasound (CEUS) that uses microbubbles as contrast agent can be used to assess the changes in vasculature. Because of the physical size of the microbubbles they remain in the intravascular space and thus, unlike DCE-MRI images, the contrast enhancement in CEUS images arises only from the tumour vasculature and there is no extravascular signal. Although CEUS can be used to obtain quantitative perfusion information, it provides no information about permeability [30]. In this study we have used CEUS images to validate our estimation of the intravascular space in the spatial domain.

All the ultrasound imaging in this study were performed using an iU22 ultrasound system (Philips Medical Systems, Bothell, WA) with a linear array transducer (L9-3, 3-9 MHz bandwidth) operating in a mode that provides anatomic and

contrast-specific images. Definity (Lantheus Medical Imaging, MA, USA) microbubbles were used as the contrast agent. A low mechanical index (MI) of 0.05 was chosen to minimise microbubble disruption in contrast imaging. To achieve an adequate temporal resolution for tracking the contrast agent, a frame rate of 8–10 Hz was used and the imaging was performed for 3 min in all studies. The CEUS dataset was acquired with temporal resolution of 100–125  $\mu$ s and the voxel size of the images was 136  $\mu$ m in both axial and lateral directions.

## MRI

The *in vivo* DCE-MRI was performed at a 1.5-T MR system (Signa, GE Healthcare, USA) using a 5-inch surface RF receive coil. A total of 150 images were acquired using an axial 2D FSPGR sequence with TR=5.3 ms, TE=1.5 ms, flip angle=30, Nx/Ny/NEX=128/128/4, BW=15.63 kHz, slice thickness=4 mm, FOV=15 cm. The DCE-MRI datasets had in-plane resolution of 1,100  $\mu$ m and temporal resolution of 2.7 s. Gd-DTPA-BMA (Omniscan, GE Healthcare, USA) was used as the contrast agent both in the phantom and *in vivo*.

The phantom was imaged with the same 1.5 T MR system as the *in vivo* study, using a custom-mode single channel RF receive coil with the following imaging parameters: TR=12.5 ms, TE=2.9 ms, flip angle=20, Nx/Ny/NEX=256/256/5, BW=15.67 kHz, slice thickness=5 mm, FOV=

45 mm. DCE-MRI data were reconstructed in two different resolutions, a high-resolution dataset with in-plane resolution=175  $\mu$ m and a low-resolution dataset with in-plane resolution=700  $\mu$ m. Both datasets had a temporal resolution of 3.2 s.

## Validation studies in a micro-vascular phantom

A phantom was constructed to mimic the behaviour of contrast agent in the microvasculature and to serve as a validation platform for the ICA analysis performed in subsequent animal studies. The phantom design was such that the true intravascular (AIF) component was available for assessment of the performance of the ICA-based method.

The MR compatible phantom (Fig. 1a) comprised of dialysis tubing (Diapes PES-150, Baxter, ID=200  $\mu$ m, wall thickness=30  $\mu$ m) through which contrast agents could flow, embedded into an agar gel matrix (0.5%, Sigma-Aldrich, Canada). In this configuration, the dialysis tubing represented the leaky microvascular compartment of tissue, and the agar gel the extravascular component. The dialysis tubes were arranged into a square grid (10  $\times$  10, centre-to-centre spacing of 300  $\mu$ m) and were aligned parallel to each other over a distance of approximately 5 cm. The pore size of the dialysis tubing ranged from 89 to 972 nm, which

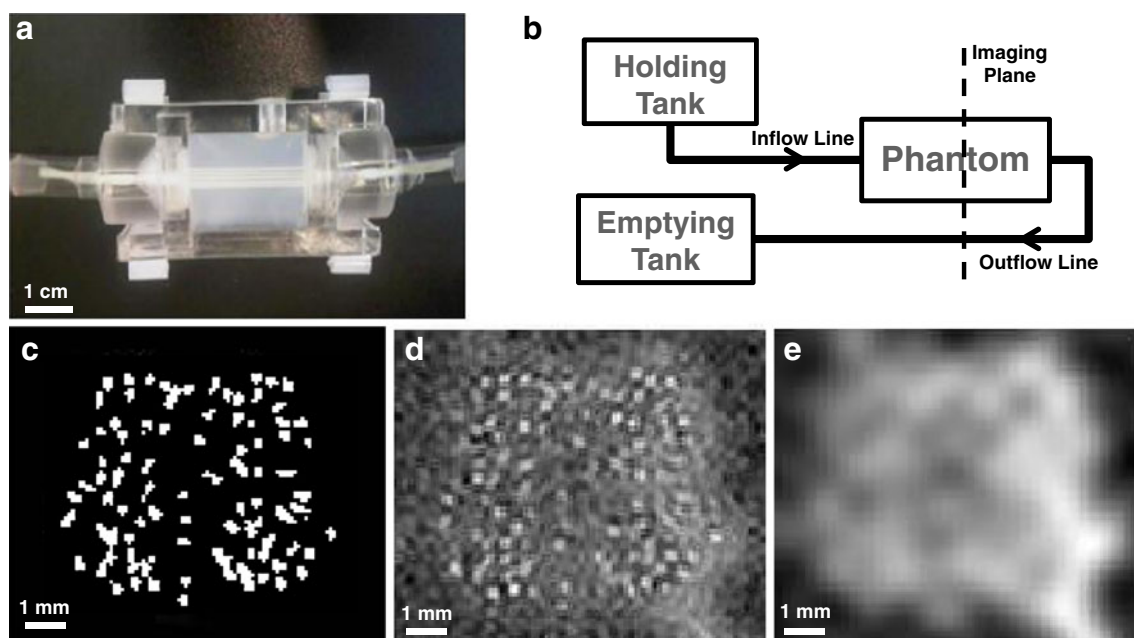


**Fig. 1** This figure shows the tissue mimicking phantom and its DCE-MRI datasets. **a** Top-view of the microvascular phantom that was constructed to mimic leaky tumour vasculature with exchange of contrast agent between the two spaces during DCE-MRI. **b** The schematic of the imaging plane showing how the phantom and the outflow line are arranged to lie in the imaging plane. **c** A binary mask generated

by thresholding a high-resolution pre-contrast image of the phantom (during flow of water through the tubes that was used to identify the voxels within the lumen of the tubes) showing the location and arrangement of the tubes in the phantom. **d** A sample frame of the high resolution DCE-MRI data of the phantom, **e** A sample frame of the low resolution DCE-MRI data of the phantom

enabled the low-molecular-weight Gd-DTPA contrast agent to diffuse out of the tubes and into the surrounding gel.

A fixed-height reservoir of water was used to produce a constant flow through the phantom at a rate of 0.047 ml/s at an input pressure of  $\sim 35.6$  mmHg, which achieved a flow velocity within the arteriole's physiological range [31]. An automatic syringe pump (Harvard Pump 11 Plus, Harvard Apparatus, Holliston, USA) was used to inject a bolus of contrast agents into the flow line in order to achieve a constant injection rate and volume. MR images were obtained transverse to the tubes during the passage of the respective contrast agents. The flow line was arranged such that the outflow tubes passed through the transverse slice as shown in Fig. 1b. The average signal in the outflow

tubes was used as the actual AIF signal of the phantom (with an 18.4-s delay). The delay corresponded to the time that it took for the contrast agent to travel from the imaging plane in the phantom to the cross-section of the outflow line that was in the imaging plane.

The DCE-MR images of the phantom were reconstructed at two different resolutions. High-resolution images were generated using the full k-space data that were acquired (FOV=45 mm, in-plane resolution=175  $\mu\text{m}$ ), and low-resolution images were generated (FOV=45 mm, in-plane resolution=700  $\mu\text{m}$ ) by removing the high-frequency components of k-space prior to image reconstruction. The high-resolution images (Fig. 1d) enabled the voxels within and outside the tubes to be spatially resolved in the phantom, while

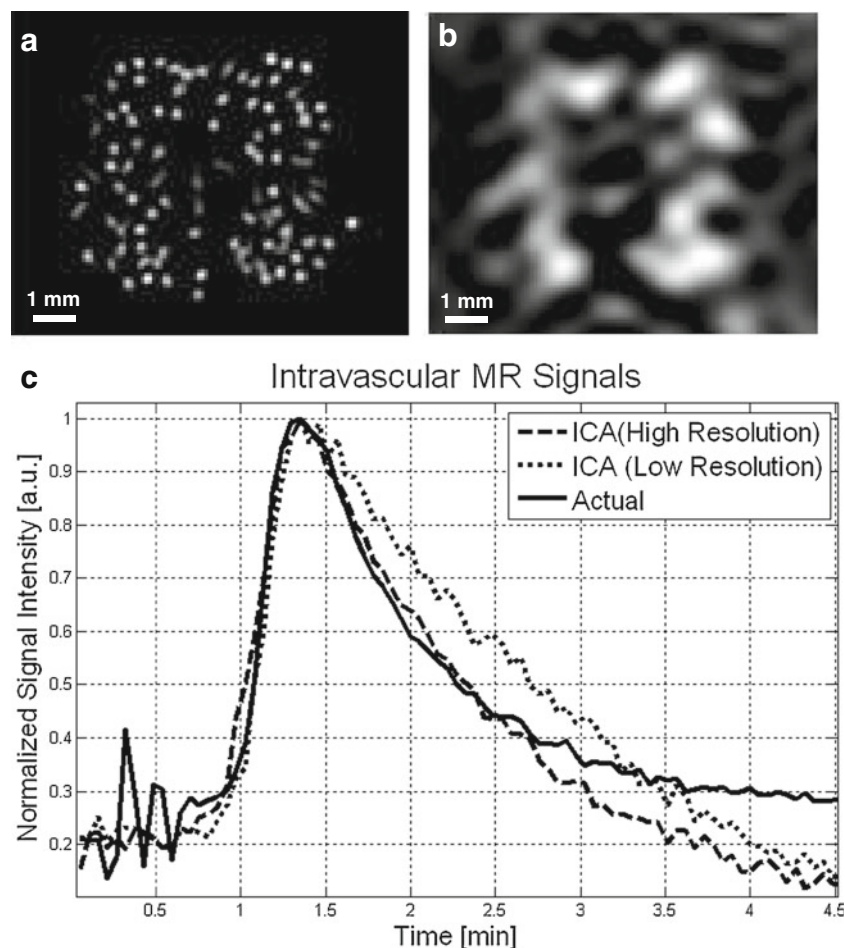


**Fig. 2** Results of applying the ICA-based method to the phantom data. **a** The tubes image obtained using ICA-based method for the high-resolution dataset. **b** The tubes image obtained using the ICA-based method for the low-resolution dataset. **c** The time-intensity curves corresponding to the tubes obtained by the ICA-based method in both high-resolution and low-resolution datasets as well as the time-intensity curve of the outflow tubes (after correcting for its delay) that is used as the actual tubes signal. The ICA-derived curves are very similar to the outflow curve, i.e. their onset time, peak time and full width at half maximum (FWHM) are very close.

This figure shows that the ICA-based method is capable of separating the tubes from the DCE-MR images of the phantom with high accuracy. It also demonstrates the robustness of the method in dealing with datasets with different resolutions particularly low-resolution ones that are expected in clinical trials. The images in **a** and **b** are thresholded by removing the voxel that enhance less than 50% of the maximum intensity value to better visualise the enhancing areas (corresponding to the tubes). The time-intensity curves are normalised with respect to their maximum values to enable comparison

the low-resolution images (Fig. 1e) simulated a typical spatial resolution obtained in clinical imaging.

#### In vivo study: animal preparation and imaging

Approval was obtained from local Animal Care Committee at Sunnybrook Health Sciences Centre for this study, which was performed in four New Zealand white rabbits (3–4.5 kg) (Charles River Laboratories, Wilmington, MA). Tumours were initiated in both thighs of rabbits through intramuscular implantation of VX2 cells as explained in [32]. Fresh tumour was initially harvested within 30 min after killing a live carrier and was cryopreserved for subsequent multiple transplantations. For each transplantation, the cryopreserved tumour was brought to room temperature and then grounded and homogenised. Viability of cells was estimated by Trypan Blue exclusion and the number of cells in suspension was counted under a microscope.

The tumours were implanted into each animal by using approximately 0.15 ml tumour suspension ( $4 \times 10^6$  cells) injected slowly via an 18-gauge needle into the musculature of the rabbit thigh. Imaging was performed approximately 13 days after implantation to enable tumours to grow to a desired volume of 1.5 cm<sup>3</sup>. Rabbits were anaesthetised with an intramuscular injection of ketamine (50 mg/kg) and xylazine (10 mg/kg). Anaesthesia was maintained during imaging using inhalation of isoflurane (3–4%). The animals were killed after imaging by intracardiac injection (Euthanyl™).

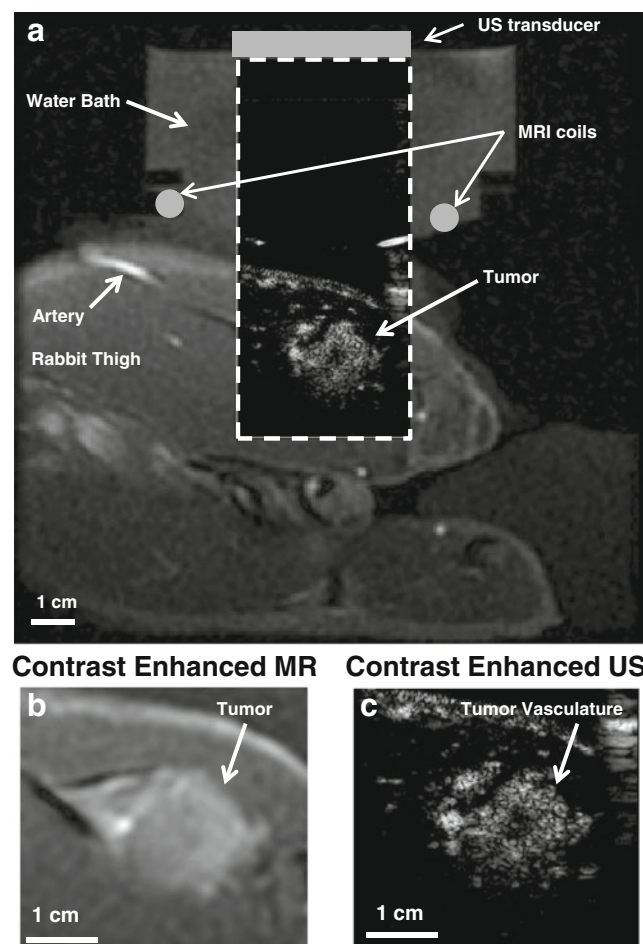
Imaging was performed with the rabbits in the lateral decubitus position, using an apparatus developed for co-registered ultrasound and MR imaging, described previously [33–35]. Briefly, ultrasound imaging was first performed to obtain 20 axial images (2 mm apart). Out of the 20 imaging planes, two suitable imaging planes were selected where a combination of tissues (tumour tissue, muscle, fat and vessels) were visible. After ultrasound imaging, the rabbits were transferred in the co-registration apparatus to a 1.5-T MRI system (Signa, GE Healthcare, USA) and MR images were obtained in the same orientation and locations as the ultrasound data. The selection of the two imaging planes was enforced by the co-registration system developed by Chandrana et al. [33].

**Table 1** The correlation coefficient between the normalised intravascular time-intensity curves (AIF) extracted by ICA and the actual curve measured at the outflow tubes (after correcting for the delay) and the *P* values, assessing how good the ICA curves fit the actual AIF curve for both high-resolution and low-resolution datasets

	Correlation coefficient	<i>P</i> value
High resolution	0.97	0.002
Low resolution	0.94	0.018

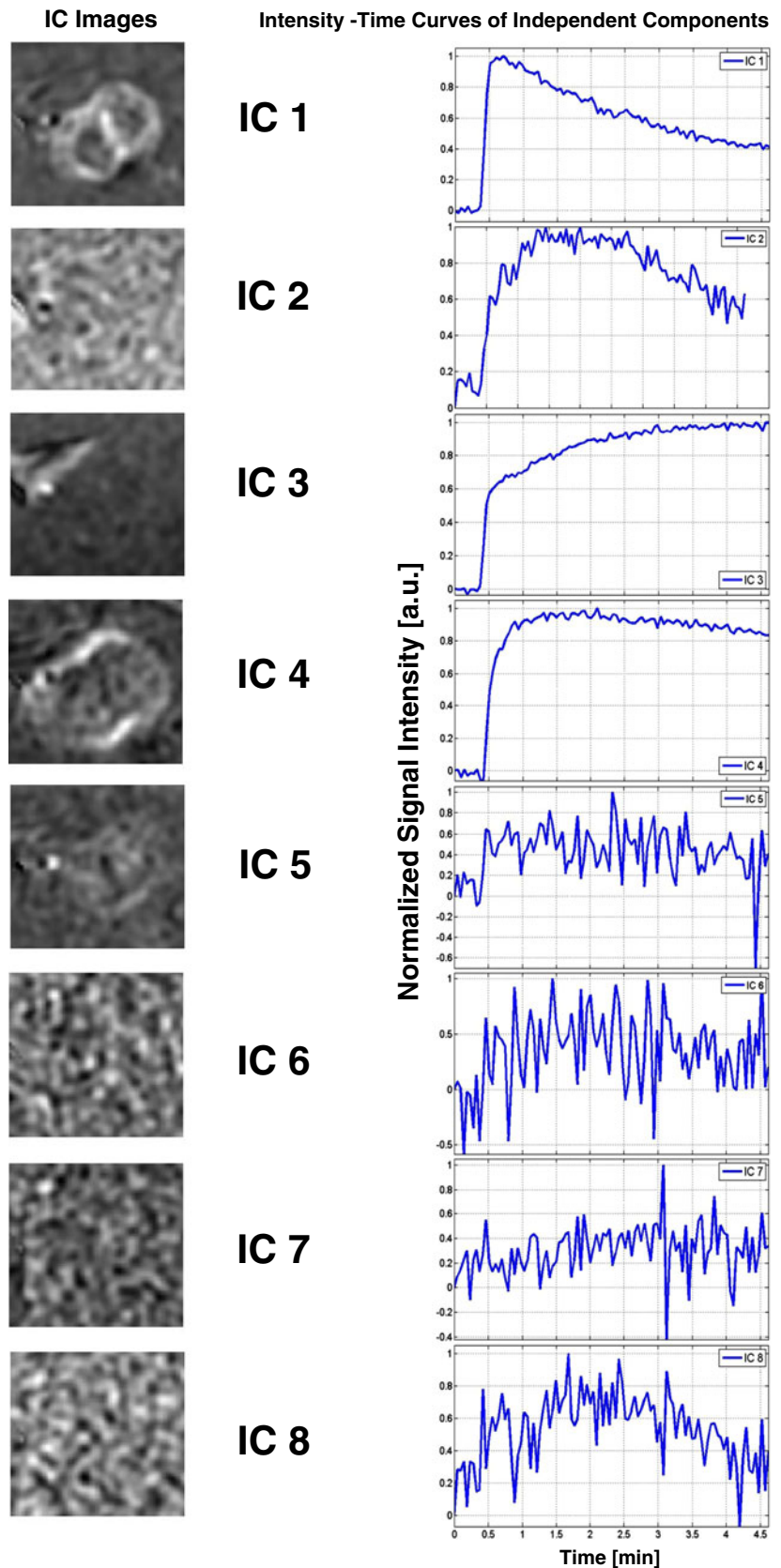
Since the ultrasound and MR acquisitions were not performed simultaneously, the set-up had two fiducials that were used to co-register the CEUS and DCE-MR images of each tumour.

In order to synchronise the contrast injections for different modalities, the following steps were taken: (1) contrast agents were injected 15 s after the start of data collection, and (2) the contrast injection volumes, flush rate and flush volume were kept the same (using injection pumps) to



**Fig. 3** The DCE-MRI and ultrasound data that was acquired in vivo. **a** This image shows the full field of view of axial MR image of the thigh of the tumour-bearing rabbit with the co-registered ultrasound image superimposed (inside the dotted line). This image also shows the artery that was identified in the imaging plane. The time-intensity curve of this artery was used as the actual AIF in our analysis to validate our separation results. **b** The co-registered images of the rabbit thigh (an area around the tumour) in DCE-MRI and **c** contrast-enhanced ultrasound (CEUS). It can be seen in these images that the contrast ultrasound and contrast MR modalities are complementary to each other. MR shows the soft tissue more clearly, while ultrasound shows a well-defined vascular network. This figure shows the ultrasound and MR datasets were correctly acquired in the plane and the co-registration process was able to align them with good accuracy to be used for validation. Moreover, some of the imaging specifications such as the location of the two RF coils that were used for MRI and the location of ultrasound transducer as well as the water bath are shown in this figure

**Fig. 4** The results of applying ICA to the tumour dataset that was shown in Fig. 3. This figure shows the intermediate steps of the ICA-based method and illustrated the process of identifying the AIF. The figure shows the eight spatially independent component images (8 eigenvalues were kept in the dimensionality reduction step) on the left column, and the corresponding temporal components on the right column (these curves are normalised with respect to their maximum values). The only temporal curve that had the pre-contrast, uptake and wash-out phases and in the wash-out phase its value dropped to 60% of the peak value, i.e had a typical intravascular enhancement curve, was component number 1. Thus, this component was selected as the intravascular component and its time-intensity curve was used as the tumour's arterial input function (AIF)



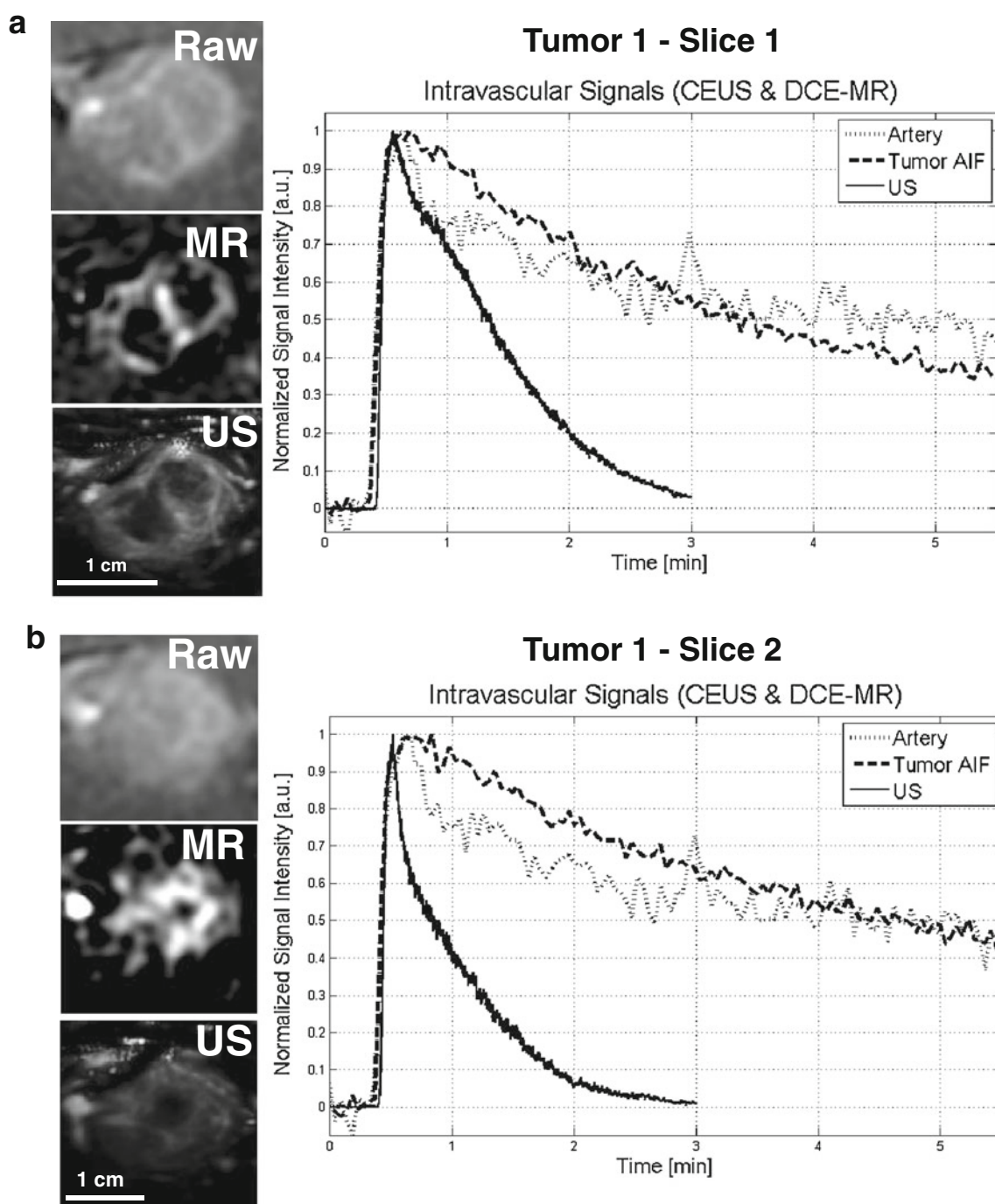


**Fig. 5** Results of applying the ICA-based method to a DCE-MR data in the tumour area of the same data as shown in Fig. 3 in (a) Slice 1 and (b) Slice 2 of the tumour. This figure shows a sample frame of the raw data (*Raw*), the intravascular component (*MR*) that was identified and separated using the ICA-based method in the spatial domain and the corresponding ultrasound image for both slices. The ultrasound image (*US*) is averaged over time, thus the noise is suppressed and the regions that have higher signal intensity (brighter regions) correspond to the areas that have more blood vessels and therefore more contrast. The plots show the normalised time-intensity curves of the intravascular space (AIF) obtained by ICA-based method, the actual AIF measured at the artery that is close to the tumour and the contrast enhancement of the tumour in the ultrasound dataset for both slices. The curves are

normalised to their maximum value and are corrected for their pre-contrast enhancement to enable comparison. The intravascular MR images are thresholded by removing the voxels that enhance less than 50% of the maximum intensity value to better visualise the enhancing areas. This figure shows that the intravascular MR curve is similar to the actual AIF (measured from the artery) and the intravascular MR image (*MR*) is similar to the tumour's corresponding ultrasound image which is purely intravascular. It also shows that the contrast uptake kinetics are similar in the actual AIF and ICA-derived AIF and these parameters are similar to those of the ultrasound curve (up to its peak value). Therefore, ICA is capable of separating the intravascular signal with reasonable accuracy

ensure rabbit's physiological reactions due to external injections were consistent. Additional parameters used for MR and ultrasound contrast imaging are detailed in [33]. The thigh muscles of four rabbits with implanted tumours were imaged with both MR and ultrasound, and contrast kinetics were studied in two imaging planes.

A large artery close to the tumour was identified in the imaging field of view of one of the tumours and was used to validate the separation results of our method. This artery was oriented such that it was parallel to the imaging plane. It also extended towards the tumour, which suggested that it was probably feeding the tumour. These characteristics made this artery a good candidate to be used as the actual AIF signal (such an artery was not present in the other datasets).

## Results

### Phantom validation study

The ICA-based method was applied to the DCE-MR images of the tissue-mimicking phantom to identify the signal originating from the tubes (AIF) and to separate it from the signal of the contrast agent leaking to the gel. The ICA-derived AIF signal was compared with the actual AIF signal that was measured at the outflow tubes to validate performance of the method. The ICA-based method was developed using MATLAB (The MathWorks, Natick, USA) software and was applied to the DCE-MRI datasets on a Pentium IV PC with 3.00 GHz Core2 CPU and 3 GB of RAM.

The method was run on both high- and low-resolution datasets, to evaluate its ability to identify the tubes' signal as well as its robustness in handling a low-resolution dataset, and the results are shown in Fig. 2. A binary mask was generated to show the location of the tubes inside the phantom by thresholding a high-resolution pre-contrast MR image of the phantom (Fig. 1c). This mask was generated to be compared with the tubes image identified by ICA (Fig. 2a) for the high-resolution dataset (the comparison is not possible for low-resolution dataset in spatial domain as the tubes cannot be visualised). Although the high- and low-resolution datasets look very different spatially, their time-intensity curves (AIF) are similar. The intra-vascular curves that were automatically extracted using ICA agree well with the curve that is measured at the outflow line (the delay in the outflow signal is corrected for in order to enable comparison); the onset times and time to peak intensity are very close for the ICA curves and the outflow curve. The curves are highly correlated and the *P* values, assessing how good the ICA-derived AIF fits the actual (outflow) AIF are less than 5% as reported in Table 1. Figure 2 and Table 1 show that the results of performing the separation on both high-

and low-resolution data were similar and were very close to the actual intravascular (tubes) signal that resulted from outflow tubes.

### Tumour studies

The VX2 tumours in rabbits were imaged with DCE-MRI and CEUS for all four rabbits (two planes were imaged for each tumour) and the images of the two modalities were co-registered [33]. Figure 3a shows the full field of view for co-registered ultrasound and MR images of one of the rabbits. A large artery was also identified in this dataset whose signal enhancement was used as the actual AIF of the animal and was used to evaluate the performance of the ICA-based method (such an artery was not present in other datasets). The reduced field of view comparisons of different acquisitions (ultrasound and MRI) are shown in Fig. 3b, c.

The deflationary ICA was applied to the dataset after dimensionality reduction and all independent components ( $n=8$  in this case) were extracted. Figure 4 shows the extracted independent components in both spatial and temporal domains (the curves are normalised with respect to their maximum value and their pre-contrast intensities are corrected for to enable comparison); in this particular dataset only component number one was selected as the intravascular component according to the criterion defined in the "Materials and methods" section.

Figure 5a shows a sample frame of the DCE-MR images of the tumour (raw data), along with its identified intravascular component using the ICA-based method. It shows the corresponding co-registered ultrasound image as well, which has been averaged over time to reduce noise and to show the areas that are enhancing. Figure 5a also shows the normalised time-intensity curves of the identified AIF, DCE-MRI signal of the artery that was detected in the imaging plane (the delay in its onset time was corrected for in order to enable comparison of the curves) and the enhancement curve from the CEUS data. The pre-contrast signal intensities of all curves are corrected for and are normalised with respect to their maximum values to enable comparison of their respective enhancements. All three curves show a similar onset time and peak time of enhancement, and the actual AIF (measured in the artery) and ICA-

**Table 2** The correlation coefficient between the normalised intravascular time-intensity curve extracted by ICA and the normalised AIF measured from the artery that is located near the tumour (actual AIF) and the *P* values, assessing how good the ICA curves fit the actual AIF for both planes of the tumour

	Correlation coefficient	<i>P</i> value
Tumour 1, Slice 1	0.92	0.04
Tumour 1, Slice 2	0.96	0.03

derived AIF show similar wash-out of contrast agent, as would be expected. Also expected is the different rate of decay of the DCE-MRI signals compared with the ultrasound curve, likely due to the different clearance mechanisms and rates for the two contrast agents as well as their half-lives. These curves and images are shown for the second slice of the same tumour, in Fig. 5b. For both slices of

this tumour, the actual AIF and the tumour AIF obtained using ICA are highly correlated and the  $P$  values, assessing how good the ICA curves fit the actual AIF curve, are less than 5%, as reported in Table 2.

The ICA-based separation method was applied to all eight datasets (four tumours and two slices for each tumour). For seven datasets, the method succeeded in identifying and

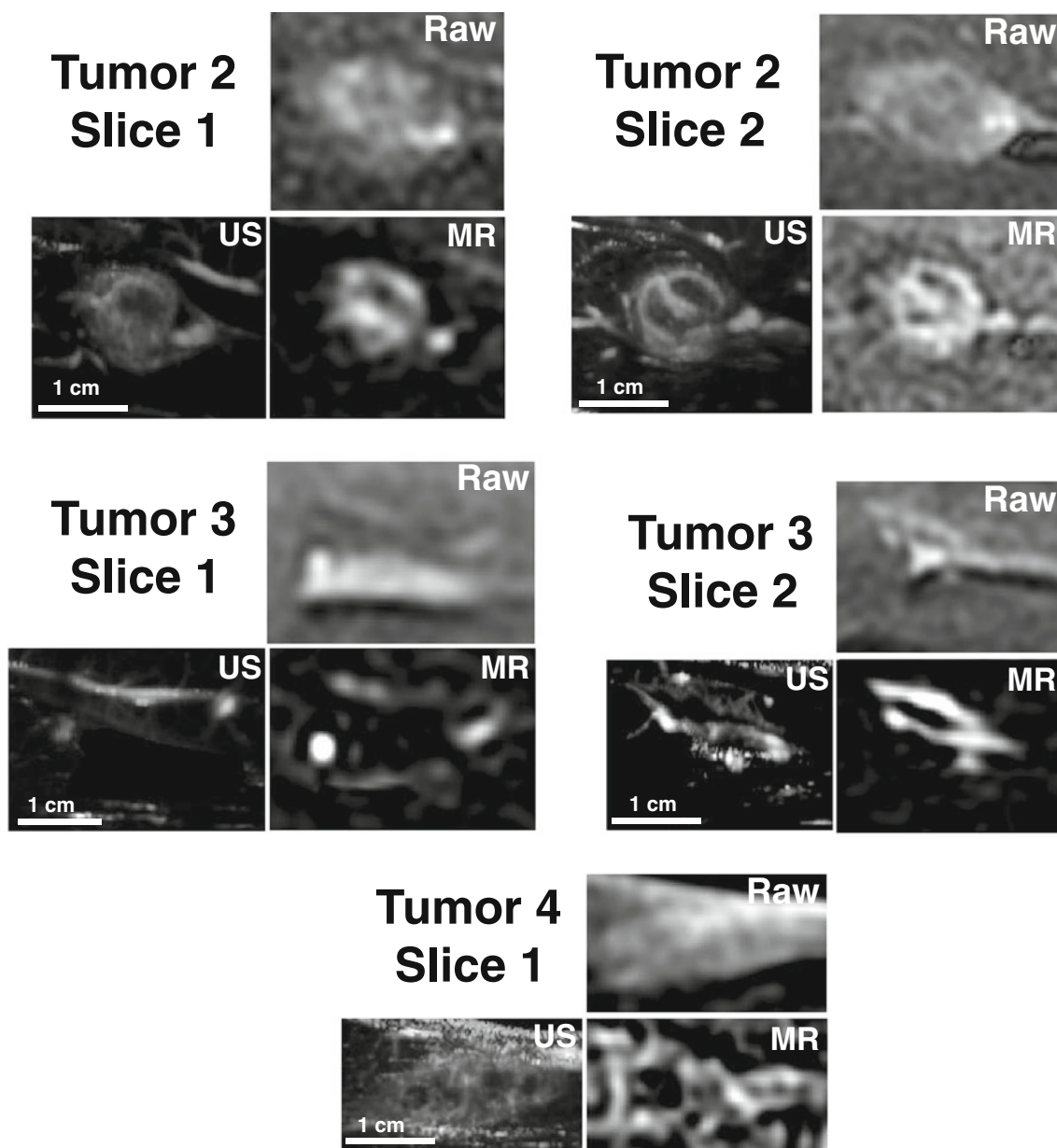


**Fig. 6** Results of applying the proposed separation method to five other DCE-MRI datasets. For each dataset, a sample frame of the raw data (*Raw*), the intravascular component image (MR) that was identified and separated using ICA-based method are shown. In addition, the corresponding ultrasound image (*US*) of each dataset that shows the intravascular components of the tissue (the ultrasound data is averaged over time to reduce noise and show the regions that enhance better) is shown. The method was applied to the eight available tumour datasets. In seven out of eight datasets the method succeeded in identifying AIF

and separating the intravascular space from the dataset. Results for five datasets (other than the two datasets that were shown in Fig. 5) are shown in this figure. The intravascular MR images are thresholded by removing the voxels that enhance less than 50% of the maximum intensity value to better visualise the enhancing areas. This figure shows the reproducibility of the method in calculating AIF in vivo. In the dataset that the method failed to calculate AIF, the imaging parameters were modified to achieve higher temporal resolution, which resulted in poor image quality (low SNR)

separating the AIF. It failed for one of the datasets where the DCE-MR imaging protocol was adjusted to a lower signal-to-noise ratio (SNR) compared with the other seven ones (3.4-times lower SNR), in an attempt to acquire images at a higher rate (NEX=1, temporal resolution=0.9 s). Therefore, the image quality of the failed dataset was much lower than the other datasets and the method was not able to separate the AIF.

Figure 6 shows the performance of the method on five other datasets (other than the two datasets that were shown in Fig. 5). This figure shows the co-registered contrast ultrasound image of the tumour and ICA-derived intravascular component. Table 3 reports the onset time (the time point at which contrast agent arrives in the tumour) and the peak time (the time point at which signal intensity reaches its maximum value) of ultrasound and intravascular MR time-intensity curve for both imaging slices of all eight in vivo datasets (there was no visible artery in MRI slices of other datasets to be compared with the tumour AIF and thus no correlation coefficients or *P* values could be calculated).

## Discussion

In a pharmacokinetic model, the determination of vascular parameters relies on accurate measurement of the contrast agent concentration in the plasma volume (AIF) [15]. However, measuring such a signal in the tumour is usually impossible. Currently the AIF is approximated outside the tumour, which may result in inaccurate PK parameters and makes the governing equation complicated. Current AIF measurement techniques have several disadvantages. In many tumours a feeding artery for the tumour in the imaging field of view does not exist, which makes PK analysis difficult and inaccurate, if not impossible. A standard AIF assumes a pre-defined theoretical form for the AIF, which is not necessarily correct and does not account for variability between individuals. Population-averaged AIF requires

measuring AIF in a number of patients for the tumour that is being studied, which is difficult and does not account for variability between patients and heterogeneity of the tumour vasculature. Reference-tissue-based techniques require that the PK parameters of normal tissues surrounding the tumour are known a priori and only provide an approximation to the AIF.

The proposed ICA-based separation method provided promising results in identifying and extracting the AIF. ICA algorithms have been applied to DCE-MRI in previous studies, but validation of the separation achieved by the algorithm is difficult and usually not addressed [36]. ICA has also been applied to AIF measurement in brain perfusion studies [37]; however, this is a less complex problem than the one we addressed in this study, as the presence of the blood-brain barrier minimises the extravascular contrast enhancement. The separation of intravascular and extravascular components in tumour studies using ICA has not been addressed before.

The initial results obtained in the microvascular phantom demonstrated the ability of the method in separating the signal from within the dialysis tubes (Fig. 2). It also showed the robustness of the method in dealing with low-resolution DCE-MR data where these compartments could not be physically separated by voxel boundaries. Similar results were seen in vivo, where the ICA-based method was able to produce intravascular images of tumours that had a striking resemblance to the contrast ultrasound images (actual intravascular image). The accuracy of the proposed method was demonstrated by comparing its separated AIF curves with an arterial enhancement (DCE-MRI) from an artery close to the tumour and with their corresponding CEUS time-intensity curves as shown in Fig. 5 and reported in Table 2.

Figure 6 and Table 3 show the results of applying the separation to all datasets. The method succeeded in separating the two spaces in seven (out of eight) datasets. The dataset that the method failed on had a higher temporal resolution and thus a much lower SNR. We are currently in the process of evaluating how the method would work on

**Table 3** The onset time (the time point at which contrast agent arrives in the tumour) and the peak time (the time point at which signal intensity reaches its maximum) of ultrasound and intravascular MR time-intensity curves for both imaging slices of all four tumours

	Onset time (min)		Peak time (min)	
	Intravascular MR	Ultrasound	Intravascular MR	Ultrasound
Tumour 1, Slice 1	0.32	0.41	0.65	0.55
Tumour 1, Slice 2	0.37	0.38	0.60	0.51
Tumour 2, Slice 1	0.50	0.57	0.89	0.80
Tumour 2, Slice 2	0.43	0.55	0.75	0.75
Tumour 3, Slice 1	0.31	0.38	0.54	0.54
Tumour 3, Slice 2	0.31	0.38	0.54	0.54
Tumour 4, Slice 1	0.39	0.39	0.56	0.52
Tumour 4, Slice 2	Failed			

datasets acquired with lower temporal resolution. As shown in Fig. 5, the method appears to be capable of separating the intravascular space of in vivo datasets. The ICA-derived AIF is very similar to the AIF that was measured in the artery which was located near the tumour. The phantom and in vivo studies show that the ICA-based method can improve the extraction of the AIF, which is required for PK modelling.

In practice, the main limitation of the method arises from the ICA assumption that the intra- and extra-vascular signals are linearly combined to form the images. There are different tissue types in each MR voxel and their signals contribute to its average MR signal. Even within a single tissue type in a voxel, there will be a small range of magnetic field strengths due to varying molecular environment of spins and proximity to other tissue types. Thus, their magnetisation vectors might not be in-phase. Since magnitude of MR signal is used here, as a result of this intra-voxel de-phasing, linear mixture assumption of ICA might be violated. This intra-voxel de-phasing can be reduced by shortening the echo time (TE) and we used a short TE to minimise it.

Further considerations are required before applying the proposed method in clinical practice, as we have assumed that  $T_1$  signal enhancement is linearly related to contrast concentration. However, this is only true for low concentrations of Gd-DTPA [38]. We also performed signal separation in the MR magnitude data; thus, our signal intensity based AIF has to be converted to contrast concentration before being used in PK analysis. This is not a trivial process and is currently under investigation. Further research is required to assess the effects of these issues and find the optimal imaging parameters and contrast specifications.

Moreover, due to the low temporal and spatial resolution of the images in clinical practice and the fact that the intravascular and extravascular spaces have to be spatially independent or their enhancements have to be distinct enough temporally to be separated by ICA, it is required to measure the lowest spatial and temporal resolutions for which the proposed method succeeds in calculating AIF.

In conclusion, we have demonstrated that ICA has the potential to identify and separate the intravascular signal in DCE-MRI. This may improve the results of conventional PK analysis, as it allows an arterial input function to be estimated automatically from the tumour. This shows the potential of this approach in cancer imaging, where it is impossible to find an ROI that identifies and separates the intravascular signal and there might not exist an artery in the imaging field of view.

**Acknowledgements** This study was conducted with the financial support of the Ontario Institute for Cancer Research (OICR) through funding provided by the Government of Ontario and the support of the Natural Sciences and Engineering Research Council of Canada (NSERC).

## References

- Weber WA (2009) Assessing tumour response to therapy. *J Nucl Med* 50:1S–10S
- Lee CH, Braga L, de Campos RO, Semelka RC (2011) Hepatic tumour response evaluation by MRI. *NMR Biomed* 24:721–733
- Forner A, Ayuso C, Varela M et al (2009) Evaluation of tumour response after locoregional therapies in hepatocellular carcinoma: are response evaluation criteria in solid tumours reliable? *Cancer* 115:616–623
- Hutchings M, Barrington SF (2009) PET/CT for therapy response assessment in lymphoma. *J Nucl Med* 50:21S–30S
- Hamstra DA, Rehemtulla A, Ross BD (2007) Diffusion magnetic resonance imaging: A biomarker for treatment response in oncology. *J Clin Oncol* 25:4104–4109
- Smith JJ, Sorensen AG, Thrall JH (2003) Biomarkers in imaging: realizing radiology's future. *Radiology* 227:633–638
- Korporaal JG, Vanvulpen M, Vandenberg CAT et al (2012) Tracer kinetic model selection for dynamic contrast-enhanced computed tomography imaging of prostate cancer. *Invest Radiol* 47:41–48
- Lawaczek R, Jost G, Pietsch H (2011) Pharmacokinetics of contrast media in humans: model with circulation, distribution, and renal excretion. *Invest Radiol* 46:576–585
- Kanematsu M, Osada S, Amaoka N et al (2005) Expression of vascular endothelial growth factor in hepatocellular carcinoma and the surrounding liver and correlation with MRI findings. *AJR Am J Roentgenol* 184:832–841
- Leach MO, Brindle KM, Evelhoch JL et al (2005) Assessment of antiangiogenic and antivascular therapies in early-stage clinical trials using magnetic resonance imaging: issues and recommendations. *Br J Cancer* 92:1599–1610
- Gossmann A, Helbich TH, Kuriyama N et al (2002) Dynamic contrast-enhanced magnetic resonance imaging as a surrogate marker of tumour response to anti-angiogenic therapy in a xenograft model of glioblastoma multiforme. *J Magn Reson Imaging* 15:233–240
- Galbraith SM, Maxwell RJ, Lodge MA et al (2003) Combretastatin A4 phosphate has tumour antivascular activity in rat and man as demonstrated by dynamic magnetic resonance imaging. *J Clin Oncol* 21:2831–2842
- Tofts P, Brix G, Buckley D et al (1999) Estimating kinetic parameters from dynamic contrast-enhanced T(1)-weighted MRI of a diffusible tracer: standardized quantities and symbols. *J Magn Reson Imaging* 10:223–232
- Naish JH, Kershaw LE, Buckley DL et al (2009) Modeling of contrast agent kinetics in the lung using T(1)-weighted dynamic contrast-enhanced MRI. *Magn Reson Med* 61:1507–1514
- Cheng HLM (2008) Investigation and optimization of parameter accuracy in dynamic contrast-enhanced MRI. *J Magn Reson Imaging* 28:736–743
- Hansen AE, Pedersen H, Rostrup E et al (2009) Partial volume effect (PVE) on the arterial input function (AIF) in T1-weighted perfusion imaging and limitations of the multiplicative rescaling approach. *Magn Reson Med* 62:1055–1059
- McGrath DM, Bradley DP, Tessier JL et al (2009) Comparison of model-based arterial input functions for dynamic contrast-enhanced MRI in tumour bearing rats. *Magn Reson Med* 61:1173–1184
- Weinmann H, Laniado M, Mutzel W (1984) Pharmacokinetics of GdDTPA/dimeglumine after intravenous injection into healthy volunteers. *Physiol Chem Phys Med NMR* 16:167–172
- Shukla-Dave A, Lee N, Stambuk H et al (2009) Average arterial input function for quantitative dynamic contrast enhanced magnetic resonance imaging of neck nodal metastases. *BMC Med Phys* 9:4

20. Yu YM, Jiang QA, Miao YW et al (2010) Quantitative analysis of clinical dynamic contrast-enhanced MR imaging for evaluating treatment response in human breast cancer. *Radiology* 257:47–55
21. Thacker NA, Williamson DC, Pokric M (2004) Voxel based analysis of tissue volume from MRI data. *Br J Radiol* 77:S114–S125
22. Ballester MAG, Zisserman AP, Brady M (2002) Estimation of the partial volume effect in MRI. *Med Image Anal* 6:389–405
23. Mehrabian H, Pang I, Chandrana C et al (2011) Automatic mask generation using independent component analysis in dynamic contrast enhanced-MRI. *Biomedical Imaging: From Nano to Macro, 2011 IEEE International Symposium, Chicago*, pp 1657–1661
24. Comon P (1994) Independent component analysis. A new concept? *Signal Process* 36:287–314
25. Araujo A, Giné E (1980) The central limit theorem for real and Banach valued random variables. Wiley, New York
26. Hyvärinen A (1999) Fast and robust fixed-point algorithms for independent component analysis. *IEEE Trans Neural Networks* 10:626–634
27. Hyvärinen A, Oja E (2000) Independent component analysis: Algorithms and applications. *Neural Netw* 13:411–430
28. Mehrabian H, Lindvere L, Stefanovic B et al (2012) A constrained independent component analysis technique for artery-vein separation of two-photon laser scanning microscopy images of the cerebral microvasculature. *Med Image Anal* 16:239–251
29. Lu W, Rajapakse JC (2005) Approach and applications of constrained ICA. *IEEE Trans Neural Networks* 16:203–212
30. Williams R, Hudson JM, Lloyd BA et al (2011) Dynamic microbubble contrast-enhanced US to measure tumour response to targeted therapy: a proposed clinical protocol with results from renal cell carcinoma patients receiving antiangiogenic therapy. *Radiology* 260:581–590
31. Ritschel WA, Kearns GL (1999) Handbook of basic pharmacokinetics—including clinical applications. American Pharmaceutical Association, Washington
32. Curiel L, Huang Y, Vykhodtseva N et al (2009) Focused ultrasound treatment of VX2 tumours controlled by local harmonic motion. *Phys Med Biol* 54(11):3405–3419
33. Chandrana C, Bevan P, Hudson J et al (2011) Development of a platform for co-registered ultrasound and MR contrast imaging in vivo. *Phys Med Biol* 56(3):861–877
34. Curiel L, Chopra R, Hynynen K (2007) Progress in multi-modality imaging: truly simultaneous ultrasound and magnetic resonance imaging. *IEEE Trans Med Imaging* 26(12):1740–1746
35. Viallon M, Terraz S, Roland J et al (2010) Observation and correction of transient cavitation-induced PRFS thermometry artifacts during radiofrequency ablation, using simultaneous ultrasound/MR imaging. *Med Phys* 37(4):1491–1506
36. Koh TS, Thng CH, Ho JTS et al (2008) Independent component analysis of dynamic contrast-enhanced magnetic resonance images of breast carcinoma: a feasibility study. *J Magn Reson Imaging* 28:271–277
37. Calamante F, Mørup M, Hansen LK (2004) Defining a local arterial input function for perfusion MRI using independent component analysis. *Magn Reson Med* 52:789–797
38. Canet E, Douek P, Janier M et al (1995) Influence of bolus volume and dose of gadolinium chelate for first-pass myocardial perfusion MR imaging studies. *J Magn Reson Imaging* 5:411–415